Hindawi Publishing Corporation
International Journal of Photoenergy
Volume 2012, Article ID 469178, 12 pages
doi:10.1155/2012/469178

Research Article

Sol-Gel-Hydrothermal Synthesis of the Heterostructured TiO_2/N-Bi_2WO_6 Composite with High-Visible-Light- and Ultraviolet-Light-Induced Photocatalytic Performances

Jiang Zhang,[1] Zheng-Hong Huang,[1] Yong Xu,[2] and Feiyu Kang[1]

[1] *Laboratory of Advanced Materials, Department of Materials Science and Engineering, Tsinghua University, Beijing 100084, China*
[2] *Department of Technology, Beijing Tongfang Puri-Tech Co., Ltd., Beijing 100083, China*

Correspondence should be addressed to Zheng-Hong Huang, zhhuang@mail.tsinghua.edu.cn
and Feiyu Kang, fykang@mail.tsinghua.edu.cn

Received 15 July 2011; Accepted 22 August 2011

Academic Editor: Jinlong Zhang

The heterostructured TiO_2/N-Bi_2WO_6 composites were prepared by a facile sol-gel-hydrothermal method. The phase structures, morphologies, and optical properties of the samples were characterized by using X-ray powder diffraction (XRD), scanning electron microscopy (SEM), high-resolution transmission electron microscopy (HRTEM), energy dispersive spectroscopy (EDS), and UV-vis diffuse reflectance spectroscopy. The photocatalytic activities for rhodamine B of the as-prepared products were measured under visible and ultraviolet light irradiation at room temperature. The TiO_2/N-Bi_2WO_6 composites exhibited much higher photocatalytic performances than TiO_2 as well as Bi_2WO_6. The enhancement in the visible light photocatalytic performance of the TiO_2/N-Bi_2WO_6 composites could be attributed to the effective electron-hole separations at the interfaces of the two semiconductors, which facilitate the transfer of the photoinduced carriers.

1. Introduction

In the past decades, TiO_2, as an effective photocatalyst with a band gap of 3.2 eV, has been widely investigated in environmental remediation and solar utilization, owing to its effectiveness, cheapness, and chemical stability. However, its low visible light response and high photoinduced charge combination limited the utilization of solar energy. To date, most of research on photocatalysis was focused on the development of novel photocatalysts with high visible light responsivity. Very recently, Bi_2WO_6 with high visible light responsivity was widely investigated to degrade organic dye waste water [1–3] and decompose volatile gaseous pollutant [4]. Bi_2WO_6 is regarded as a promising visible light photocatalyst for dealing with the environmental problems in water and air due to its narrow band gap. Unfortunately, the low photocatalytic performance of Bi_2WO_6 was caused by its poor adsorption property and weak migration of photoinduced charge carriers.

To improve the photoactivity of Bi_2WO_6, hierarchical nest-like structure [5] and hierarchical flowers [6] with a hollow structure were constructed by solution self-assembly of nanoplates, providing high surface area and porous structure for adsorption of organic molecules. As is well known, high photoinduced charge recombination is a harmful factor to photocatalytic activity of Bi_2WO_6. The "Schottky" barrier between the metal and the semiconducting photocatalyst was considered to be an efficient path to improve the interfacial charge transfer process and accelerate the charge carrier separation. Bi_2WO_6/Cu^0 [7] with Fenton-like synergistic effect and Bi_2WO_6/Ag^0 [8] heterojunctions were designed to prevent the electron-hole recombination and improve the photocatalytic performance. In addition, carbon-modified Bi_2WO_6 [9, 10] was also considered to enhance the photoactivity due to high specific surface area and high conductivity of carbon, accelerating the charge transfer from photocatalyst to the liquid-solid interface contacted with organic pollutants by making use of carbon's unique electron transport properties. Heterostructured Bi_2WO_6-TiO_2 composite [11, 12] was discovered to possess the synergetic effect between TiO_2 and Bi_2WO_6 which leads to an effective charge

carrier separation, exhibiting the outstanding photocatalytic performance under sunlike irradiation.

In our experiments, nitrogen-doped Bi_2WO_6 was synthesized by a hydrothermal method in the first step. And then nanosized TiO_2 particles were coated on the surface of N-doped Bi_2WO_6 nanoplates by a facile sol-gel-hydrothermal process. The influences of nitrogen doping on the structure, optical properties, and morphologies of Bi_2WO_6 were investigated. And the mechanism of enhanced photocatalytic activities of TiO_2/N-Bi_2WO_6 was explained by nitrogen doping and the synergetic effect between TiO_2 and N-doped Bi_2WO_6.

2. Experimental

2.1. Synthesis of N-Doped Bi_2WO_6. All the reagents were of analytical purity and were used as received from Shanghai Chemical Company. Similar to the reported experiments [13], in a typical procedure, aqueous solutions of 10 mmol $Bi(NO_3)_3 \cdot 5H_2O$ and 5 mmol $Na_2WO_4 \cdot 2H_2O$ were mixed together, then the mixture was magnetic stirred for two hours at room temperature. Afterward, aqueous solution containing desired amounts of urea ($CO(NH_2)_2$) was added for N-doped Bi_2WO_6 with the atomic ratio of N to Bi in 0.5 in the precursor. Then, the suspension was added into a 50 mL Teflon-lined autoclave up to 80% of the total volume. The suspension in the autoclave was heated at 160°C for 24 h. Subsequently, the autoclave was cooled to room temperature. The products were collected by filtration and then were washed by deionized water. The samples were then dried at 80°C for several hours and were denoted as N-BWO.

2.2. Preparation of the Heterostructured TiO_2/N-Bi_2WO_6 Composites. The heterostructured TiO_2/N-Bi_2WO_6 composite was synthesized via a sol-gel-hydrothermal process. Briefly, a mixed solution of 20 mmol of $Ti(OC_4H_9)_4$, 183 mmol of ethanol (C_2H_5OH), and 1 g of the as-prepared N-doped Bi_2WO_6 was magnetic stirred for 30 minutes, forming a homogeneous mixed suspension. Subsequently, a mixed solution of 183 mmol of ethanol (C_2H_5OH), 75 mmol of H_2O, and 2.8 mmol HNO_3 was dropped into the above suspension and magnetic stirred for another 30 minutes to get a highly dispersed gelatin. As-obtained gelatin was aged for a whole night and was transferred into the autoclave of 50 mL with 15 mL H_2O at 160°C for 24 h, denoted as TiO_2/N-BWO. The resultant samples were calcined at 400°C for 1 h, 2 h (5°C/min) to remove solvents and other organic species, which were denoted as TiO_2/N-BWO-400/1 h, TiO_2/N-BWO-400/2 h, respectively. For comparison, the pristine $Bi_2WO_6$was synthesized by a hydrothermal process at 160°C for 24 h, denoted as BWO. And the pure TiO_2 was fabricated via a sol-gel-hydrothermal method at 160°C for 24 h, denoted as H-TiO_2.

2.3. Catalyst Characterization. The crystalline phases of the as-prepared catalysts were confirmed by powder X-ray diffraction (XRD). The XRD patterns were obtained for the heterostructured TiO_2/N-Bi_2WO_6 samples by using a Rigaku Multiflex diffractometer at 40 kV and 200 mA with monochromated high-intensity CuKα radiation. The surface morphology of the as-synthesized samples was observed by a field emission scanning electron microscope (FE-SEM). High-resolution transmission electron microscopy (HRTEM) was performed on JEOL-2010F operated at 200 kV. To prepare the transmission electron microscopy (TEM) sample, a small amount of samples was ultrasonically dispersed in ethanol. A drop of such suspension was placed on a 200-mesh Cu grid with holey carbon film and dried completely in air. The UV-vis diffuse reflectance spectra (DRS) were acquired on a Shimadzu UV-2450 spectrophotometer with ISR-240A integrating sphere assembly in the range of 200–800 nm. $BaSO_4$ was used as a reflectance standard.

2.4. Evaluation of Photocatalytic Activity. The photocatalytic performance of the heterostructured TiO_2/N-Bi_2WO_6 samples was evaluated by decomposing rhodamine B (RhB) under visible and ultraviolet light irradiation at room temperature. A 300 W Xe lamp (CEL-HXB UV300, Beijing China Education Au-light Co., Ltd.) equipped with an ultraviolet cutoff filter to provide visible light ($\lambda > 420$ nm) was used as the visible light source, and which equipped with an ultraviolet reflected filter to provide ultraviolet light ($\lambda < 400$ nm) was regarded as the ultraviolet light source. And the distance between the liquid surface of the suspension and the light source was set about 7 cm. The photodegradation experiments were carried out with the sample powder (50 mg) suspended in RhB aqueous solution (100 mL, 4×10^{-5} mol L^{-1}) with constant magnetic stirring. Prior to the irradiation, the suspensions were magnetically stirred in the dark for 2 h to establish the adsorption/desorption equilibrium. At the given time intervals, about 4 mL of the suspension was taken for further analysis after centrifugation. RhB photodegradation was analyzed by recording the absorbance at the characteristic band at 553 nm as a function of irradiation time on a UV-vis spectrophotometer (Shimadzu UV 2450).

3. Results and Discussion

3.1. XRD Patterns of TiO_2/N-Bi_2WO_6 Composites. The phase structures of as-prepared samples were investigated using powder X-ray diffraction. The XRD patterns for the heterostructured anatase TiO_2/N-Bi_2WO_6 composites are shown in Figure 1(a). For comparison, the XRD patterns of the pure Bi_2WO_6, N-doped Bi_2WO_6, and the pure TiO_2 are also given. It is observed that the as-prepared pure Bi_2WO_6 powder was in good agreement with the standard orthorhombic phase of Bi_2WO_6 (JCPDS no. 39–0256), while diffraction peaks of H-TiO_2, corresponding to the standard tetragonal phase of anatase (JCPDS no. 21–1272), were clearly observed. No new crystal orientations or changes in preferential orientations of N-doped Bi_2WO_6 are observed comparing to pure Bi_2WO_6, despite of the presence of doping with nitrogen. However, the diffracted intensity of (131) crystallographic plane displays an obvious decrease owing to the doping of nitrogen. And the widening diffraction peak of (131) crystallographic plane of N-doped Bi_2WO_6

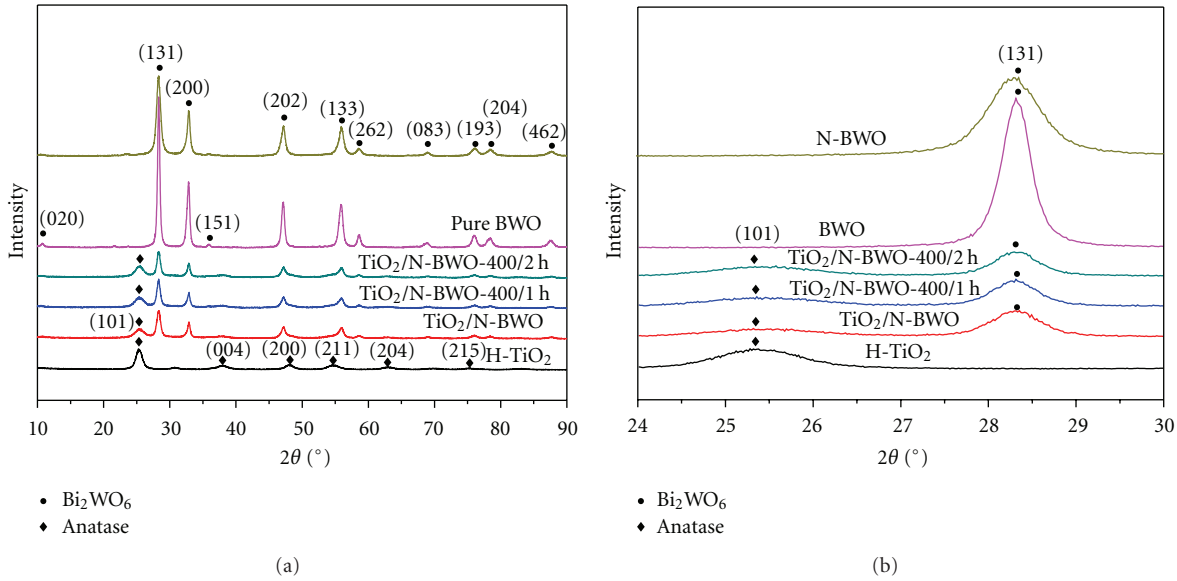

Figure 1: XRD patterns of TiO_2/N-BWO, TiO_2/N-BWO-400/1 h, TiO_2/N-BWO-400/2 h, BWO, N-BWO, and H-TiO_2.

is induced by the doping of nitrogen in Figure 1(b). In addition, the peak position of N-doped Bi_2WO_6 shifts slightly toward a lower 2θ value. In the XRD patterns for the heterostructured TiO_2/N-Bi_2WO_6 composites, the anatase phase TiO_2 peak of (101) crystallographic plane gradually appeared and the diffracted intensity of N-doped Bi_2WO_6 drastically decreased in Figure 1(a). After the heat treatment, the phase compositions of the as-prepared composites do not change any, indicating that N-Bi_2WO_6 plays a suppressive role in the phase transformation from anatase to rutile phase of TiO_2. Highly dispersed TiO_2 coated on the surface of N-Bi_2WO_6 resulted in the weak peaks corresponding to N-Bi_2WO_6 and anatase TiO_2 which were observed in the heterostructured TiO_2/N-Bi_2WO_6 composites. The average crystal grain sizes of the as-prepared products are calculated from (131) crystallographic plane in Figure 1(b) according to the Scherrer formula and are summarized in Table 1. It is found that, for the pure Bi_2WO_6, the average crystal grain size is about 20.67 nm, while the average crystal grain size in N-doped Bi_2WO_6 and TiO_2/N-Bi_2WO_6 decreased due to the doping with nitrogen and the suppressive effect of TiO_2 on the growth of N-Bi_2WO_6. The average crystal grain size of TiO_2 increased owing to hydrothermal reaction and postcalcination. Since the ionic radius of N^{3-} (0.171 nm) is larger than that of O^{2-} (0.140 nm) and the high electron density of N^{3-} ions, the most of N^{3-} ions were doped in the crystal lattice of Bi_2WO_6 [14]. Thus, the crystal lattice cell parameter of Bi_2WO_6 along b-axis direction has a slightly increase whereas that along c-axis direction has a slightly decrease owing to the doping with nitrogen (in Table 2).

3.2. SEM. The morphologies of the as-prepared products were characterized by SEM. As shown in Figure 2, the pure Bi_2WO_6 product is composed of the large and highly dispersed nanoplates. The platelike morphology is maintained after doping with nitrogen though the sheet sizes become much lower. Moreover, the small nanoplates become more and more aggregated. For comparison, the as-prepared TiO_2 is composed of the small anatase spherical aggregates via a hydrothermal process. The significant morphology modification is induced by the incorporation of TiO_2 into the N-doped Bi_2WO_6 structure. No distinct platelike structure in the TiO_2/N-Bi_2WO_6 is observed owing to the coating of the spherical TiO_2 particles on the surface of nanoplates. After calcination, the TiO_2 nanoparticles occur the crystal growth and the heterostructured TiO_2/N-Bi_2WO_6 displays an aggregate trend.

Table 1: Crystal sizes of the as-synthesized samples.

Sample	$D(BWO)_{(131)}$/nm	$D(TiO_2)_{(101)}$/nm
H-TiO_2	—	6.92
BWO	20.67	—
N-BWO	12.82	—
TiO_2/N-BWO	12.00	14.24
TiO_2/N-BWO-400/1 h	15.86	12.58
TiO_2/N-BWO-400/2 h	10.09	21.60

Table 2: Crystal lattice cell parameters of Bi_2WO_6 in the as-synthesized samples.

Sample	a/nm	b/nm	c/nm
BWO	5.45	16.43	5.44
N-BWO	5.45	16.44	5.44
TiO_2/N-BWO	5.44	16.48	5.43
TiO_2/N-BWO-400/1 h	5.45	16.51	5.41
TiO_2/N-BWO-400/2 h	5.45	16.44	5.41

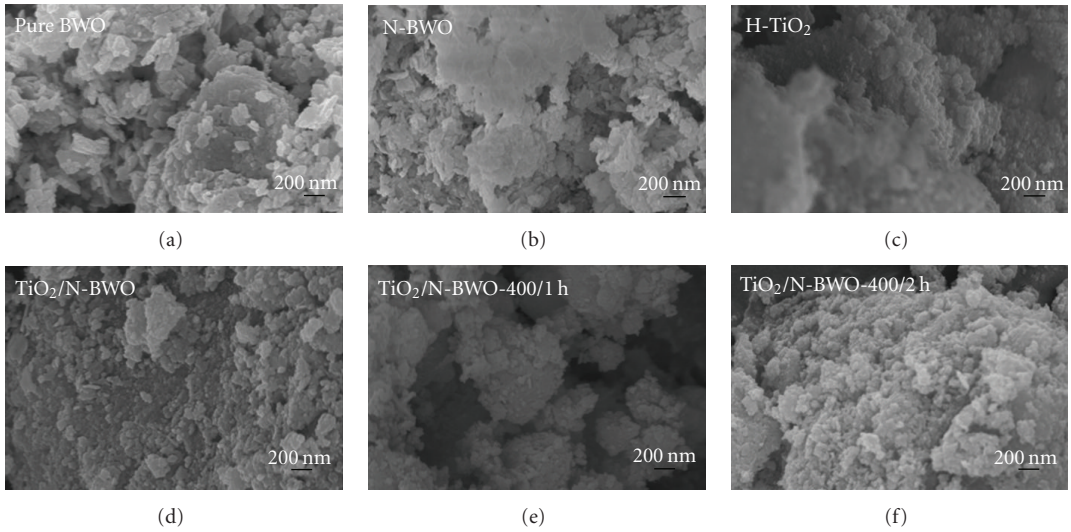

Figure 2: Selected SEM micrographs for the as-prepared samples.

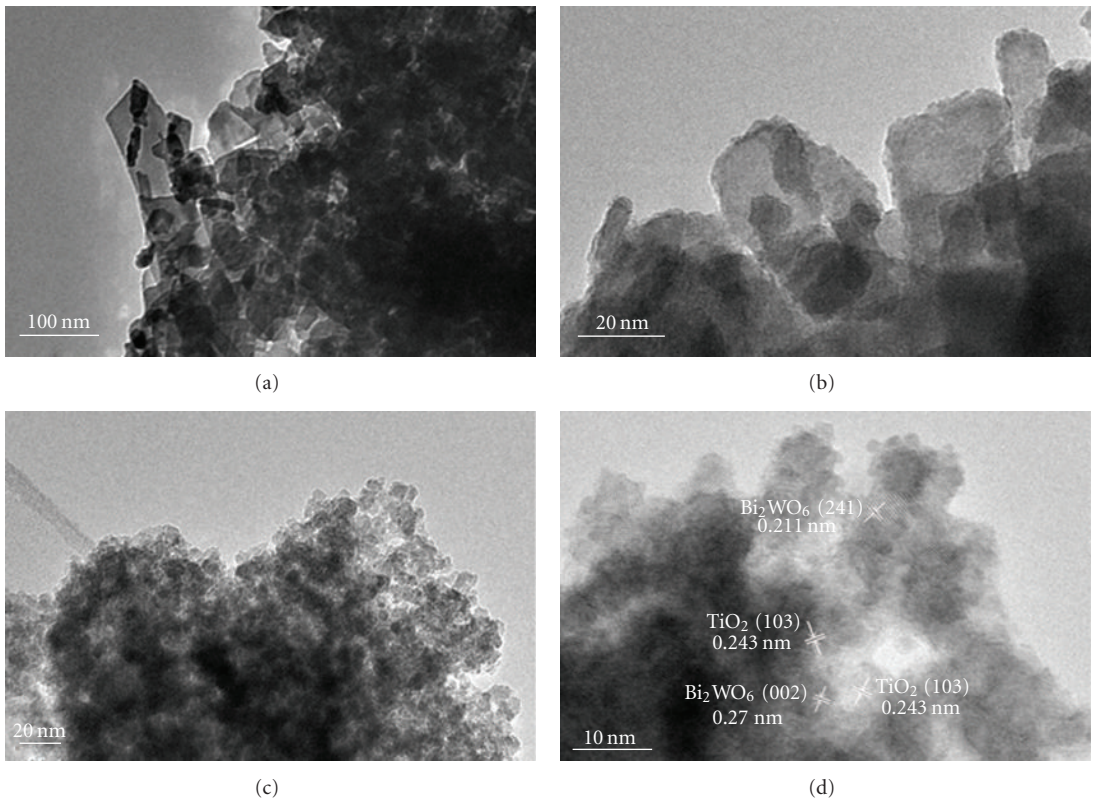

Figure 3: TEM photographs for the as-prepared N-BWO (a, b) and TiO_2/N-BWO (c, d).

3.3. TEM. To confirm the microstructure of the heterostructured TiO_2/N-Bi_2WO_6, the TEM photographs of the as-synthesized N-BWO and TiO_2/N-BWO are shown in Figure 3. These results show that the nitrogen-doped Bi_2WO_6 sample is composed of highly dispersed and homogeneous nanoplates, indicating that doping with nitrogen does not result in the change of the morphologies of Bi_2WO_6 (in Figure 3(a)). Figure 3(b) reveals that the weak crystallinity of N-BWO is obtained as a result of doping with nitrogen. The microstructure of the TiO_2/N-BWO composite was further studied by TEM and HRTEM. Figure 3(c) shows the typical TEM image of the TiO_2/N-BWO heterostructure, in which many small spherical TiO_2 nanoparticles of approximately 5–10 nm with an anatase phase are coated on the surface of the platelike N-doped Bi_2WO_6 particles. The nanoplates of N-doped Bi_2WO_6 were

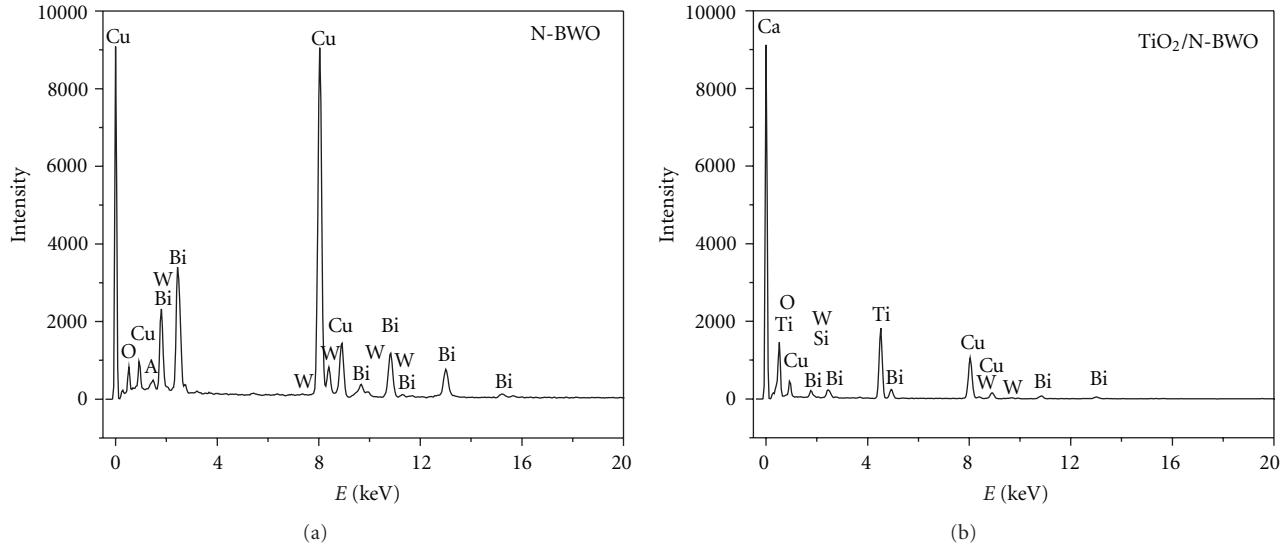

Figure 4: Energy dispersive spectra for the as-prepared N-BWO and TiO_2/N-BWO.

hardly observed in Figure 3(c), indicating that the well-coated anatase TiO_2 layer was obtained on the surface of N-doped Bi_2WO_6 nanoplates. The representative HRTEM image of the magnified view of the top right corner area is given in Figure 3(d). As can be seen, three sets of different lattice fringes were clearly observed. The lattice fringes of 0.211 nm and 0.270 nm correspond to the (241) and (002) crystallographic planes of nitrogen-doped γ-Bi_2WO_6, while the lattice fringe of 0.243 nm matches well with the (103) crystallographic plane of anatase TiO_2. The well-defined fringes and the high crystallinity of the heterostructured TiO_2/N-Bi_2WO_6 composites facilitate the separation of the photoinduced carriers, improving the corresponding photocatalytic activities [15]. The distinct interface was observed between segregated units of TiO_2 and N-doped Bi_2WO_6 nanoparticles, revealing that the heterostructure indeed formed from these two materials.

To further confirm the formation of the TiO_2/N-BWO heterostructure, the energy dispersive spectra were measured to analyze the species and contents of the as-prepared N-BWO and TiO_2/N-BWO samples. Figure 4 shows that there are some peaks of Bi, W, and O elements in the spectrum of N-BWO, while the peak of N element is not observed owing to the slightly doping with nitrogen. For comparison, the peak of Ti element is discovered except the peaks of Bi, W, and O elements. The content of each element is listed in Table 3. The atomic ratio of Bi : W : O is 2.67 : 1 : 2.31 which is different from that of pure Bi_2WO_6, indicating that the stoichiometric ratio of Bi_2WO_6 is changed by the doping with nitrogen. Moreover, small amount of residual carbon is also observed in the N-doped Bi_2WO_6 sample. Different from the situation of N-BWO, the atomic ratio of Bi : W : Ti : O of the heterostructured TiO_2/N-BWO is 3.61 : 1 : 102.87 : 97.74 due to the incorporation of anatase TiO_2. The discrepancy of the atomic ratio was induced by the thick TiO_2 coating layer which influenced the detection signal of the energy dispersive spectroscopy. This result was in accordance with the TEM observation of the existence of TiO_2 coating layer on the surface of N-doped Bi_2WO_6 nanoplates.

Table 3: Characterization data of EDS for N-BWO and TiO_2/N-BWO samples.

N-BWO		
Element	Weight ratio (%)	Atomic ratio (%)
C K	0.43	2.47
O K	0.95	4.11
Al K	0.29	0.74
Cu K	79.23	86.15
W M	4.74	1.78
Bi M	14.36	4.75
Total	100.00	
TiO_2/N-BWO		
Element	Weight ratio (%)	Atomic ratio (%)
O K	10.61	30.30
Si K	0.63	1.02
Ca K	0.37	0.42
Ti K	33.44	31.89
Cu K	48.59	34.94
W M	1.23	0.31
Bi M	5.14	1.12
Total	100.00	

3.4. Optical Properties. To evaluate the photoresponsivity, the UV-vis diffuse reflectance spectra of the as-prepared samples are investigated. As can be seen in Figure 5(a), H-TiO_2 exhibits remarkably strong absorption in the ultraviolet light region blow the wavelength of 400 nm. In contrast, the absorption edge of the pure BWO sample has an obvious red shift to approximate 460 nm in the visible light region

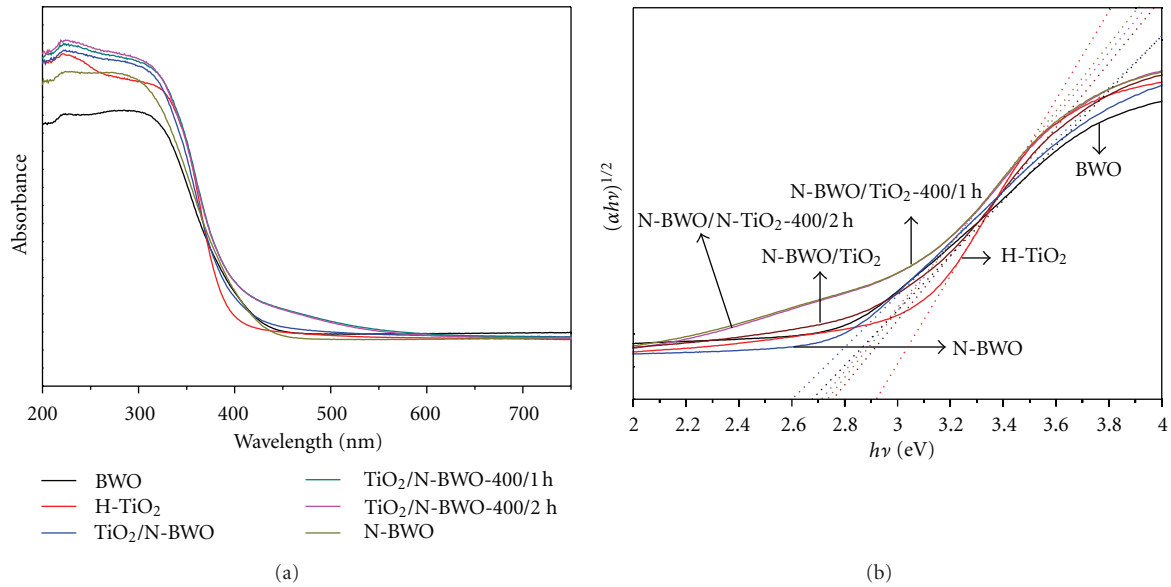

Figure 5: (a) UV-vis diffuse reflectance spectra for the as-synthesized samples. (b) The relationship between $(ahv)^{1/2}$ and photon energy.

and its ultraviolet absorption is weak. In comparison with the pure Bi_2WO_6, the N-BWO sample has a slightly red shift of the absorption edge. However, it is interesting that the absorption for the ultraviolet light greatly increased as a result of doping with nitrogen, revealing that the N-BWO sample possesses the excellent ultraviolet and visible light photoresponsivities. The absorption plots show all TiO_2/N-BWO samples exhibit a slightly blue shift of the absorption edge and have strong light response in the ultraviolet region with the addition of TiO_2 composition. In addition, with prolonging the calcination time, the absorption intensities in the visible light region increase significantly, which indicates that there is a synergetic effect on the light absorption between TiO_2 and N-doped Bi_2WO_6. Based on the equation $\alpha hv = A(hv - E_g)^{n/2}$ [16–18], the relationship between $(ahv)^{1/2}$ and photon energy is shown in Figure 5(b). And the band gaps of the as-prepared samples were estimated to be 2.92, 2.67, 2.60, 2.75, 2.73, and 2.71 eV in Table 4, corresponding to H-TiO_2, BWO, N-BWO, TiO_2/N-BWO, TiO_2/N-BWO-400/1 h, and TiO_2/N-BWO-400/2 h, respectively. From this result, it is deduced that the band gap of N-doped Bi_2WO_6 becomes much narrower owing to the influence of doping with nitrogen, whereas that of TiO_2/N-BWO composites become much wider due to the introduction of TiO_2.

3.5. Photocatalytic Activities. Figure 6 shows the photocatalytic activities of the as-prepared samples in the degradation of RhB under both ultraviolet and visible light irradiation. As can be seen in Figure 6(a), when the system was illuminated with visible light, the pure Bi_2WO_6 samples exhibited the lowest photocatalytic activity and the lowest degradation ratio of RhB. It was interesting that as-prepared H-TiO_2 exhibited a higher photocatalytic activity for the degradation of RhB, which was different from the traditional viewpoint that TiO_2 was an effective ultraviolet-light-driven photocatalyst [19, 20]. However, the nitrogen-doped Bi_2WO_6 displayed a slightly higher photocatalytic activity than both H-TiO_2, and pure BWO. This result proved that the enhanced visible light photocatalytic performance was caused by the doping with nitrogen. In the case of the heterostructured TiO_2/N-BWO composite without calcination, the highest photocatalytic activity for the degradation of RhB was obtained, which was probably caused by the effective separation of photoinduced charge carriers owing to the synergetic effect between TiO_2 and N-doped Bi_2WO_6 [21, 22]. The visible-light-induced photocatalytic activity of the heterostructured TiO_2/N-BWO composite was higher than that of the commercial P25. This indicated that the formation of the new heterostructure was beneficial to accelerating the separation of the photoinduced charges, improving the visible-light-induced photocatalytic activity. A negative influence on photocatalytic activity was induced by prolonging the calcination time. It was a probable cause that the crystal growth of TiO_2 and N-BWO resulted in the decrease of photocatalytic reactive sites. As all we know, decreased grain radius would be beneficial to reducing the recombination opportunities of the photoinduced electron-hole pairs.

Table 4: Estimation of the band gap energy of the as-prepared samples.

Sample	Band gap energy (eV)
H-TiO_2	2.92
BWO	2.67
N-BWO	2.60
TiO_2/N-BWO	2.75
TiO_2/N-BWO-400/1 h	2.73
TiO_2/N-BWO-400/2 h	2.71

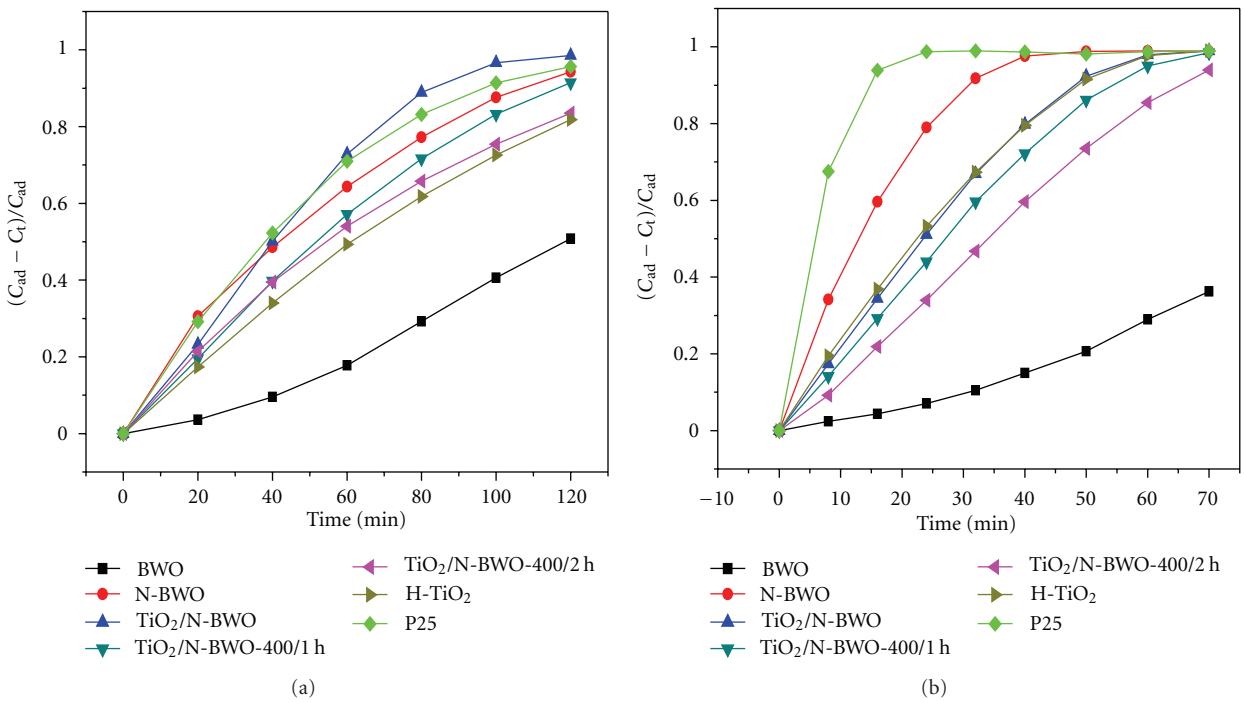

FIGURE 6: Photocatalytic activity for decomposition of rhodamine B (4×10^{-5} mol L^{-1}) under (a) visible light (>420 nm) and (b) ultraviolet light (<400 nm) irradiation at room temperature in air over the as-prepared catalysts. C_{ad}: the concentration of RhB after dark adsorption, C_t: the concentration of RhB during the photocatalytic reaction.

The photocatalytic activity was also evaluated under ultraviolet light irradiation. As shown in Figure 6(b), N-doped Bi_2WO_6 exhibited the optimal photocatalytic activity for the degradation of RhB among the as-prepared samples. The residual concentration of RhB in the solution was close to zero after photocatalytic reaction for 40 minutes. It proved that the doping with nitrogen into the crystal lattice of Bi_2WO_6 was beneficial to improving the ultraviolet-light-induced photocatalytic performance. However, it was lower than that of the commercial P25 owing to its weak ultraviolet light photoresponsivity and its large crystal size. And H-TiO_2 was found to exhibit much lower photocatalytic activity than N-doped Bi_2WO_6. However, the photocatalytic activity of H-TiO_2 under ultraviolet light irradiation was slightly higher than that of TiO_2/N-BWO. In the case of ultraviolet light illumination, the photocatalytic activity of the heterostructured TiO_2/N-Bi_2WO_6 samples was much lower than that of N-BWO. Furthermore, the photocatalytic activity of TiO_2/N-Bi_2WO_6 heterostructure become lower and lower with prolonging the calcination time under ultraviolet light illumination. This was contrary with the results of UV-vis diffuse reflectance spectra in Figure 5. These results showed that the ultraviolet-light-driven photocatalytic activities of N-BWO, H-TiO_2, and TiO_2/N-BWO decrease with the enhanced ultraviolet light photoresponsivity as shown in Figure 5. Herein, the probable cause of the decreased photocatalytic activities was relative to the increased recombination opportunities of the photoinduced charges. From SEM images in Figure 2, the obvious aggregation and the crystal growth of TiO_2 particles on the surfaces of N-doped Bi_2WO_6 particles were observed, which was adverse to the effective photoinduced charge separation. The photocatalytic activity was influenced greatly by the dispersivity and the crystal size of catalyst's particles. A better dispersivity and a smaller crystal size of the catalyst's particles were beneficial to the separation of the photoinduced electrons and holes. In the case of ultraviolet light irradiation, the TiO_2 component in the heterostructured TiO_2/N-BWO composite played the main function during the photodegradation of RhB as shown in Figure 9. The increased crystal size of TiO_2 would result in the increased recombination opportunities of the photogenerated charges consequentially. A thicker TiO_2 layer coated on the surfaces of N-doped Bi_2WO_6 particles was adverse to the utilization of the photoactivity of the N-doped Bi_2WO_6 component. Moreover, the photodegradation for RhB using N-doped Bi_2WO_6 as catalyst was incomplete, producing a large number of intermediates. The above-mentioned causes were responsible for lower photocatalytic activity of the heterostructured TiO_2/N-BWO composite without calcination under ultraviolet light irradiation, comparing with H-TiO_2 and N-doped Bi_2WO_6. Nevertheless, the pure BWO exhibited the lowest photocatalytic activity due to its weak ultraviolet light photoresponsivity. By comparison, all of the as-prepared samples exhibited higher photocatalytic activities under ultraviolet light irradiation than that under visible light irradiation.

To distinguish the photodegradation rate for RhB over the as-prepared catalysts, the kinetic-fitted curves plots of photodegradation of RhB under different light source with various wavelength ranges are displayed in Figure 7

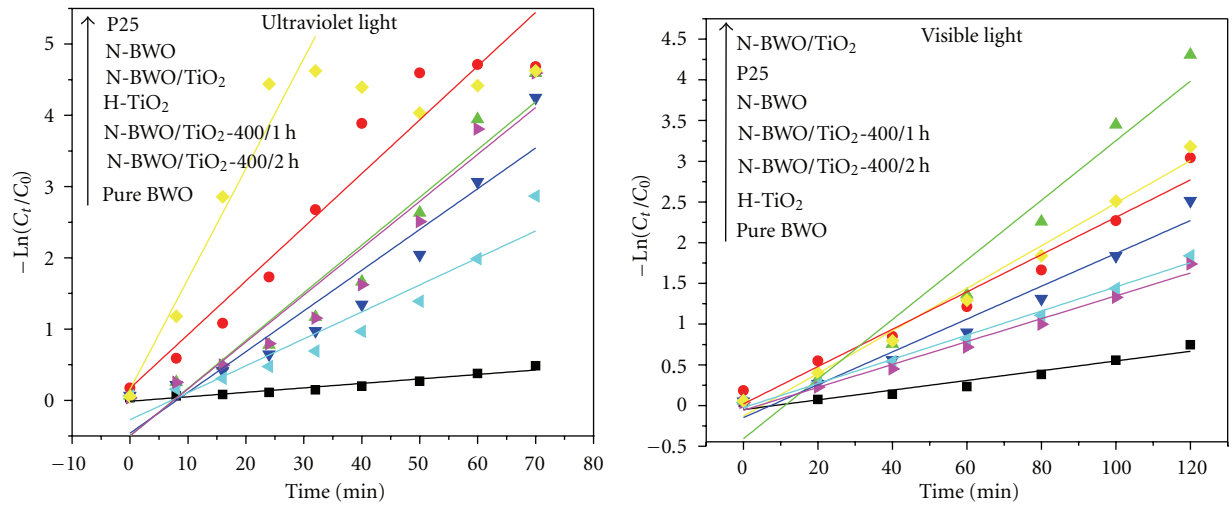

Figure 7: Kinetic fitted curves plots of photocatalytic degradation of RhB (4×10^{-5} mol L^{-1}) under ultraviolet light (<400 nm) (a) and visible light (>420 nm) (b) irradiation at room temperature in air over the as-prepared catalysts.

Table 5: The values of the photodegradation rate constant k for RhB and linearly dependent coefficient R^2.

Sample	Ultraviolet light		Visible light	
	k (mol L^{-1} min^{-1})	R^2	k (mol L^{-1} min^{-1})	R^2
$H\text{-}TiO_2$	6.58×10^{-2}	0.927	1.41×10^{-2}	0.982
BWO	6.20×10^{-3}	0.929	5.97×10^{-3}	0.931
N-BWO	7.53×10^{-2}	0.929	2.29×10^{-2}	0.964
TiO_2/N-BWO	6.69×10^{-2}	0.928	3.66×10^{-2}	0.946
TiO_2/N-BWO-400/1 h	5.71×10^{-2}	0.899	2.02×10^{-2}	0.959
TiO_2/N-BWO-400/2 h	3.78×10^{-2}	0.905	1.48×10^{-2}	0.991
P25	1.55×10^{-1}	0.945	2.61×10^{-2}	0.982

and the corresponding values of the photodegradation rate constant k for RhB and linearly dependent coefficient R^2 are listed in Table 5. The–$Ln(C_t/C_0)$ linearly increased, which meant the photodegradation of RhB under both ultraviolet and visible light irradiation over as-prepared samples could be described as first-order reaction [16]. The photocatalytic activity of the as-prepared samples can be also evaluated by the values of k, that is, the higher the value of k, the better the photocatalytic activity [23]. Moreover, the larger the coefficients R^2, the better the linear dependence relation. From the fitted results in Table 5, under ultraviolet light illumination, the order of the values of k was $1.55 \times 10^{-1} > 7.53 \times 10^{-2} > 6.69 \times 10^{-2} > 6.58 \times 10^{-2} > 5.71 \times 10^{-2} > 3.78 \times 10^{-2} > 6.20 \times 10^{-3}$, corresponding to the slopes of kinetic fitted curves of P25, N-BWO, TiO_2/N-BWO, H-TiO_2, TiO_2/N-BWO-400/1 h, TiO_2/N-BWO-400/2 h and pure BWO, respectively. The ultraviolet-light-driven photodegradation rate for RhB using the heterostructured TiO_2/N-BWO composite without calcination is much lower than that of the commercial P25. As we know, P25 was an excellent ultraviolet-light-responsive photocatalyst. Hence, the photocatalytic activity of P25 under ultraviolet light irradiation should be much higher than that under visible light irradiation. This viewpoint was proved by the comparison of Figures 6(a) and 6(b). By contrast, under visible light irradiation, the order of the values of k was $3.66 \times 10^{-2} > 2.61 \times 10^{-2} > 2.29 \times 10^{-2} > 2.02 \times 10^{-2} > 1.48 \times 10^{-2} > 1.41 \times 10^{-2} > 5.97 \times 10^{-3}$, corresponding to the slopes of kinetic-fitted curves of TiO_2/N-BWO, P25, N-BWO, TiO_2/N-BWO-400/1 h, TiO_2/N-BWO-400/2 h, H-TiO_2, and pure BWO, respectively. By comparison, the photodegradation rate for RhB under ultraviolet light irradiation was higher than that under visible light irradiation. N-doped Bi_2WO_6 exhibited the highest photodegradation rate under ultraviolet light irradiation, whereas TiO_2/N-BWO exhibited the highest photodegradation rate under visible light irradiation. Furthermore, the photodegradation rate of the heterostructured TiO_2/N-BWO composite without calcination under visible light irradiation was much higher than that of the commercial P25. This result indicated that the formation of the heterostructure facilitated the effective separation of the photoinduced charge carriers on the interface between TiO_2 and N-doped Bi_2WO_6, improving visible-light-driven photocatalytic performance.

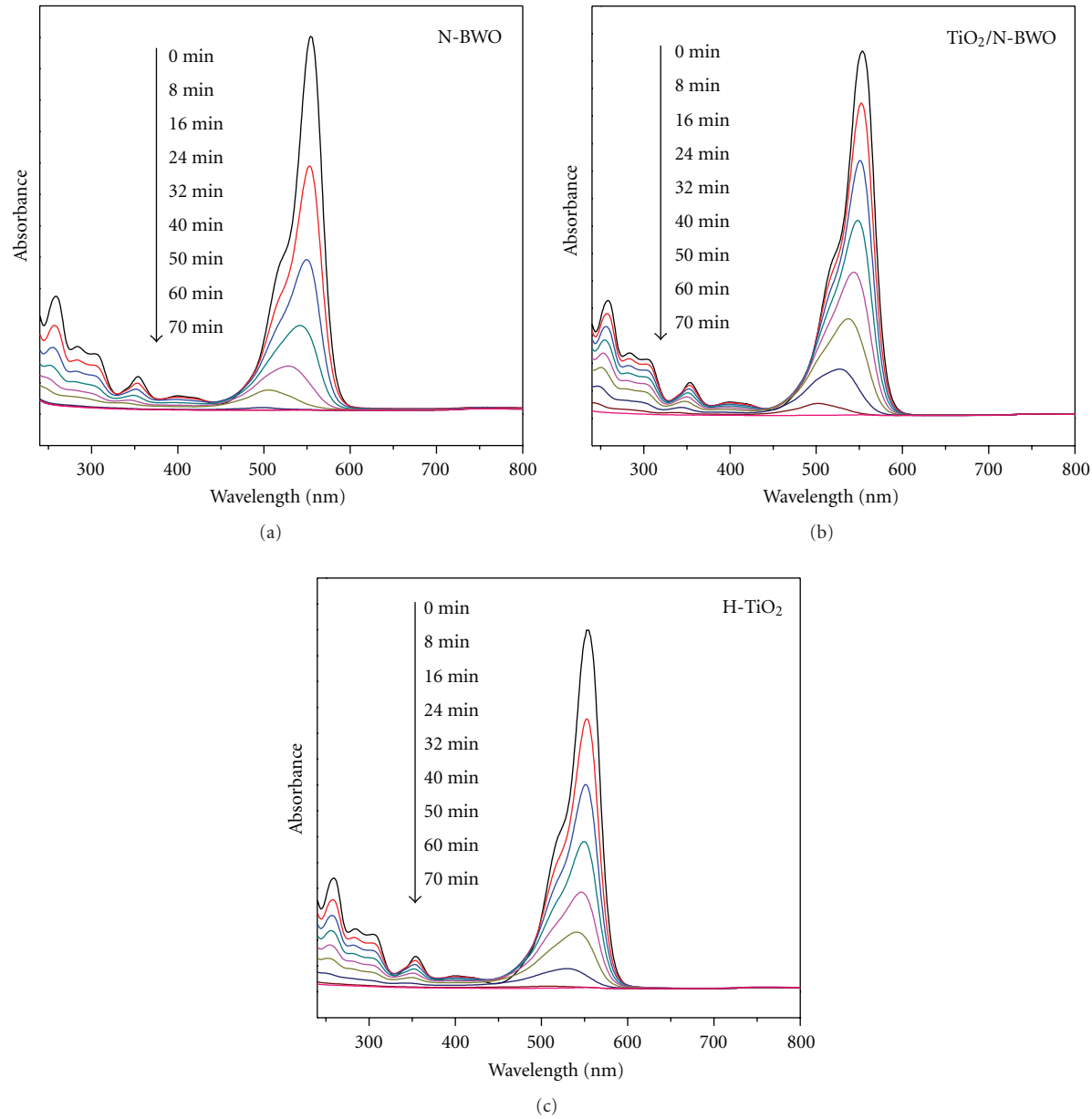

Figure 8: Temporal evolution of the spectral changes during the photodegradation of RhB over N-BWO, TiO_2/N-BWO, and H-TiO_2 under ultraviolet light irradiation.

3.6. Photocatalytic Mechanism. The temporal evolutions of the spectral changes during the photodegradation of RhB over N-BWO, TiO_2/N-BWO, and H-TiO_2 under ultraviolet light irradiation are shown in Figure 8. As all we know, RhB possesses a maximal absorption band at 553 nm. If degraded over N-doped Bi_2WO_6 under ultraviolet light irradiation for 32 minutes (in Figure 8(a)), the spectral maximum of RhB shifted from 553 to 531 nm, indicating that the mechanistic pathways of RhB degradation over N-doped Bi_2WO_6 was multisteps process accompanying with the deethylation process of the cleavage of the chromophore structure [16]. In the case of TiO_2/N-BWO (in Figure 8(b)), the deethylation function was weaken owing to the incorporation of TiO_2 with an anatase phase under ultraviolet light irradiation. Thus, the photodegradation of RhB occurred mainly by decomposing the pollutants to small molecules of CO_2 and H_2O. As for H-TiO_2 in Figure 8(c), the deethylation phenomenon was hardly seen during the degradation of RhB under ultraviolet light irradiation. By comparison, the photodegradation rate of RhB was accelerated by the doping with nitrogen into the crystal lattice of Bi_2WO_6, because the number of photoinduced electrons and holes to participate in the photocatalytic reaction was increased remarkably, resulting in the enhanced photocatalytic activity. Under ultraviolet light irradiation, the heterostructure of TiO_2/N-BWO does not significantly influence the photodegradation

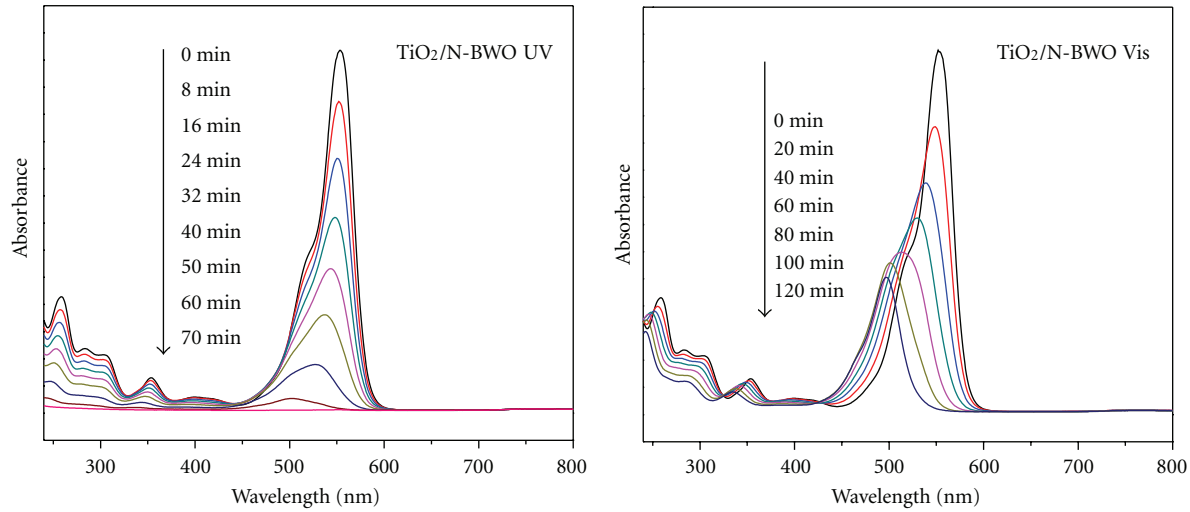

Figure 9: Temporal evolution of the spectral changes during the photodegradation of RhB over TiO_2/N-BWO under ultraviolet light irradiation (a) and visible light irradiation (b).

rate of RhB comparing to both N-BWO and H-TiO_2 due to the strong oxidation performance of H-TiO_2 with an intense ultraviolet photoresponsivity.

Based on the above discussions, the as-prepared H-TiO_2 and N-BWO were not only used as ultraviolet-light-driven photocatalysts but also regarded as visible-light-driven photocatalysts. Therefore, the heterostructure formed between H-TiO_2 and N-doped Bi_2WO_6 was expected to possess the excellent photocatalytic performances as a bifunctional photocatalyst. Thus the heterostructured TiO_2/N-BWO composite exhibited the excellent photocatalytic activities under both ultraviolet light and visible light irradiation as shown in Figure 9. Furthermore, the mechanisms of photodegradation of RhB over TiO_2/N-BWO were completely distinct under different conditions of light irradiation. In our experiments, the composition of TiO_2 in the heterostructure played an important role in the photodegradation of RhB under ultraviolet light irradiation (Figure 9(a)), while the composition of N-doped Bi_2WO_6 in the heterostructure played an important role in the photodegradation of RhB under visible light irradiation (Figure 9(b)). In addition, the photodegradation pathways of RhB were also disparate in the two cases. As for ultraviolet-light-driven photodegradation, the molecules of RhB over TiO_2/N-BWO were degraded into small inorganic molecules of CO_2 and H_2O directly. Different from the case of ultraviolet photodegradation, the decomposition of RhB over TiO_2/N-BWO was carried out step by step via a deethylation process under visible light illumination, resulting in the obvious blue shift of the maximal absorption band of RhB. The interface formed between H-TiO_2 and N-doped Bi_2WO_6 can facilitate the transportation of photoinduced charge carriers and suppress the recombination of photogenerated electrons and holes pairs, inducing the enhanced photocatalytic activity under visible light illumination.

The enhanced visible-light-driven photocatalytic performance is related to the corresponding energy band structure. The doping with nitrogen resulted in the formation of a dopant energy level at the bottom of conduction band of Bi_2WO_6. The narrowing band gap of N-BWO was beneficial to increasing the transfer rate of electrons to the photocatalyst surface, promoting photocatalytic reaction. According to the estimated Eg values of the TiO_2 and N-doped Bi_2WO_6 in Figure 5(b) and the conduction band (CB) and valence band (VB) levels of Bi_2WO_6 are lower than that of TiO_2 [11, 12], the energy band structure of TiO_2/N-BWO composite was schematically shown in Figure 10. The strong interaction between H-TiO_2 and N-BWO resulted in a synergetic effect on the photocatalytic activity of the heterostructure. The photoinduced electron-hole pairs were produced by the excitation of TiO_2/N-BWO under ultraviolet and visible light irradiation. The photoinduced electrons transferred from the conduction band of H-TiO_2 to that of N-doped Bi_2WO_6 due to the joint of the internal electric fields between two materials. However, the photoinduced holes transferred from the valence band of N-doped Bi_2WO_6 to that of H-TiO_2. Thus, the effective photoinduced charge separation provided more and more active free radicals to participate in the photocatalytic degradation of RhB. The novel design of the bifunctional TiO_2/N-BWO heterostructure provided a new approach to develop the visible-light-driven photocatalysts. But N-doped Bi_2WO_6 was more likely to be excited by visible light, being regarded as the main functional component under visible light irradiation. However, TiO_2 was more likely to be excitated by ultraviolet light, being regarded as the main functional component under ultraviolet light irradiation. Therefore, TiO_2/N-BWO composite exhibits diverse photodegradation mechanisms for RhB under different light irradiation conditions.

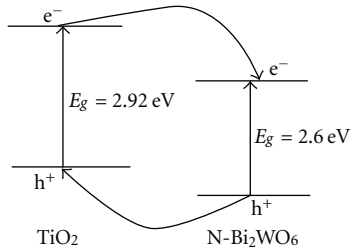

Figure 10: Schematic diagram for energy band matching and electron-hole separation.

4. Conclusion

Heterojuncted TiO_2/N-Bi_2WO_6 composites were synthesized by a facile sol-gel-hydrothermal process. The as-prepared TiO_2/N-Bi_2WO_6 composites display a wide range of light absorption due to the introduction of TiO_2, and the corresponding photocatalytic activities against rhodamine B are slightly improved in comparison with pristine Bi_2WO_6 and TiO_2. It is also found that the existence of TiO_2 in the heterojuncted TiO_2/N-Bi_2WO_6 composites plays an important role in the photocatalytic property. The enhancement in the visible light photocatalytic performance of TiO_2/Bi_2WO_6 composites can be attributed to the effective electron-hole separations at the interfaces between TiO_2 and N-Bi_2WO_6, which facilitate the transfer of the photoinduced carriers. The experiments prove that the heterojuncted TiO_2/Bi_2WO_6 composites are promising photocatalysts under visible and ultraviolet light irradiation.

Acknowledgment

The authors are grateful for the financial support by the National High Technology Research and Development Program of China (863 Program no. 2010AA064907).

References

[1] G. Zhang, F. Lü, M. Li, J. Yang, X. Zhang, and B. Huang, "Synthesis of nanometer Bi_2WO_6 synthesized by sol-gel method and its visible-light photocatalytic activity for degradation of 4BS," *Journal of Physics and Chemistry of Solids*, vol. 71, no. 4, pp. 579–582, 2010.

[2] G. Q. Zhang, N. Chang, D. Q. Han, A. Q. Zhou, and X. H. Xu, "The enhanced visible light photocatalytic activity of nanosheet-like Bi_2WO_6 obtained by acid treatment for the degradation of rhodamine B," *Materials Letters*, vol. 64, no. 19, pp. 2135–2137, 2010.

[3] Z. Cui, D. Zeng, T. Tang, J. Liu, and C. Xie, "Enhanced visible light photocatalytic activity of QDS modified Bi_2WO_6 nanostructures," *Catalysis Communications*, vol. 11, no. 13, pp. 1054–1057, 2010.

[4] Y. Chen, X. Cao, J. Kuang, Z. Chen, J. Chen, and B. Lin, "The gas-phase photocatalytic mineralization of benzene over visible-light-driven Bi_2WO_6@C microspheres," *Catalysis Communications*, vol. 12, no. 4, pp. 247–250, 2010.

[5] J. Wu, F. Duan, Y. Zheng, and Y. Xie, "Synthesis of Bi_2WO_6 nanoplate-built hierarchical nest-like structures with visible-light-induced photocatalytic activity," *Journal of Physical Chemistry C*, vol. 111, no. 34, pp. 12866–12871, 2007.

[6] S. Liu and J. Yu, "Cooperative self-construction and enhanced optical absorption of nanoplates-assembled hierarchical Bi_2WO_6 flowers," *Journal of Solid State Chemistry*, vol. 181, no. 5, pp. 1048–1055, 2008.

[7] J. Xu, W. Wang, E. Gao, J. Ren, and L. Wang, "Bi_2WO_6/Cu^0: a novel coupled system with enhanced photocatalytic activity by Fenton-like synergistic effect," *Catalysis Communications*, vol. 12, no. 9, pp. 834–838, 2011.

[8] J. Ren, W. Wang, S. Sun, L. Zhang, and J. Chang, "Enhanced photocatalytic activity of Bi_2WO_6 loaded with Ag nanoparticles under visible light irradiation," *Applied Catalysis B*, vol. 92, no. 1-2, pp. 50–55, 2009.

[9] Y. Li, J. Liu, X. Huang, and J. Yu, "Carbon-modified Bi_2WO_6 nanostructures with improved photocatalytic activity under visible light," *Dalton Transactions*, vol. 39, no. 14, pp. 3420–3425, 2010.

[10] E. Gao, W. Wang, M. Shang, and J. Xu, "Synthesis and enhanced photocatalytic performance of graphene-Bi_2WO_6 composite," *Physical Chemistry Chemical Physics*, vol. 13, no. 7, pp. 2887–2893, 2011.

[11] S. Murcia López, M. C. Hidalgo, J. A. Navío, and G. Colón, "Novel Bi_2WO_6-TiO_2 heterostructures for Rhodamine B degradation under sunlike irradiation," *Journal of Hazardous Materials*, vol. 185, no. 2-3, pp. 1425–1434, 2011.

[12] M. Shang, W. Wang, L. Zhang, S. Sun, L. Wang, and L. Zhou, "3D Bi_2WO_6/TiO_2 hierarchical heterostructure: controllable synthesis and enhanced visible photocatalytic degradation performances," *Journal of Physical Chemistry C*, vol. 113, no. 33, pp. 14727–14731, 2009.

[13] M. Shang, W. Wang, L. Zhang, and H. Xu, "Bi_2WO_6 with significantly enhanced photocatalytic activities by nitrogen doping," *Materials Chemistry and Physics*, vol. 120, no. 1, pp. 155–159, 2010.

[14] Y. Hu, D. Li, Y. Zheng et al., "$BiVO_4/TiO_2$ nanocrystalline heterostructure: a wide spectrum responsive photocatalyst towards the highly efficient decomposition of gaseous benzene," *Applied Catalysis B*, vol. 104, no. 1-2, pp. 30–36, 2011.

[15] H. Cheng, B. Huang, Y. Dai, X. Qin, and X. Zhang, "One-step synthesis of the nanostructured AgI/BiOI composites with highly enhanced visible-light photocatalytic performances," *Langmuir*, vol. 26, no. 9, pp. 6618–6624, 2010.

[16] C. Zhang and Y. Zhu, "Synthesis of square Bi_2WO_6 nanoplates as high-activity visible-light-driven photocatalysts," *Chemistry of Materials*, vol. 17, no. 13, pp. 3537–3545, 2005.

[17] H. Fu, C. Pan, W. Yao, and Y. Zhu, "Visible-light-induced degradation of rhodamine B by nanosized Bi_2WO_6," *Journal of Physical Chemistry B*, vol. 109, no. 47, pp. 22432–22439, 2005.

[18] J. Zeng, H. Wang, Y. Zhang, M. K. Zhu, and H. Yan, "Hydrothermal synthesis and photocatalytic properties of pyrochlore la $2Sn_2O_7$ nanocubes," *Journal of Physical Chemistry C*, vol. 111, no. 32, pp. 11879–11887, 2007.

[19] Y. Ao, J. Xu, and D. Fu, "Study on the effect of different acids on the structure and photocatalytic activity of mesoporous titania," *Applied Surface Science*, vol. 256, no. 1, pp. 239–245, 2009.

[20] J. T. Carneiro, T. J. Savenije, J. A. Moulijn, and G. Mul, "Toward a physically sound structure-activity relationship of TiO_2-based photocatalysts," *Journal of Physical Chemistry C*, vol. 114, no. 1, pp. 327–332, 2010.

[21] C. Yu, C. Fan, X. Meng, K. Yang, F. Cao, and X. Li, "A novel Ag/BiOBr nanoplate catalyst with high photocatalytic activity

in the decomposition of dyes," *Reaction Kinetics, Mechanisms and Catalysis*, vol. 103, no. 1, pp. 141–151, 2011.

[22] F. Duan, Y. Zheng, and M. Chen, "Flowerlike $PtCl_4/Bi_2WO_6$ composite photocatalyst with enhanced visible-light-induced photocatalytic activity," *Applied Surface Science*, vol. 257, no. 6, pp. 1972–1978, 2011.

[23] S. Zhang, C. Zhang, Y. Man, and Y. Zhu, "Visible-light-driven photocatalyst of Bi_2WO_6 nanoparticles prepared via amorphous complex precursor and photocatalytic properties," *Journal of Solid State Chemistry*, vol. 179, no. 1, pp. 62–69, 2006.